

Itinerant ferromagnetism in repulsively interacting spin-orbit coupled Fermi gas

Shang-Shun Zhang^{1,2}, Jinwu Ye^{2,3}, and Wu-Ming Liu¹

¹*Beijing National Laboratory for Condensed Matter Physics,
Institute of Physics, Chinese Academy of Sciences, Beijing 100190, China*

²*Department of Physics and Astronomy, Mississippi State University, MS 39762, USA*

³*Key Laboratory of Terahertz Optoelectronics, Ministry of Education,
Department of Physics, Capital Normal University, Beijing 100048, China*

(Dated: April 24, 2019)

We investigate the itinerant ferromagnetism of repulsively interacting Fermi gases with spin-orbit coupling (SOC). We find that the spin-orbit coupling provides a new and efficient mechanism to realize the itinerant ferromagnetism (FM) which is a long sought state in material science at much weaker repulsive interactions. We classify the symmetries and symmetry breaking of the SOC Hamiltonian and find their exact constraints on the density-spin response functions. In the para-magnet side, the SOC leads to the splitting of two transverse modes. In the FM side, the Fermi surfaces acquire a finite momentum and also experience a topological Lifshitz transition, the symmetry breaking leads to one gapped transverse pseudo-Goldstone mode instead of one gapless Goldstone mode. Various experimental probes are discussed.

PACS numbers: 03.75.Ss, 05.10.Cc, 68.35.Rh, 67.80.dk

Introduction— The investigation and control of spin-orbit (SO) coupling have become subjects of intensive research in condensed matter and cold atoms since the discovery of the topological insulators [1, 2]. It was found to be a critical factor leading to a whole new class of electronic states in *correlated* electron materials [3]. The recent experimental realizations of 1d SOC [4, 5] and the proposals to realize the 2d Rashba or Dresselhaus SOC [6] and 3d isotropic (Weyl) SOC [7] for neutral cold atoms inspired extensive theoretical investigations on various important effects of SOC on the pairing physics of attractively interacting Fermi gases [8, 9]. However, there are still relatively few works in the repulsive side which could display quite different symmetry breaking orders [10, 11].

On the other front, realizing the itinerant ferromagnetism (FM) is a long-standing goal in material science dating back to the Stoner's instability [12, 13]. There were both experimental [14] and theoretical works [15] on possible FM in a purely repulsively interacting two-component Fermi gas of ⁶Li atoms. But so far, the effects of SOC on the formation of itinerant FM have not been discussed.

In this Letter, we develop a path integral formalism [16, 17] to study itinerant FM transitions in a repulsively interacting Fermi gas with 3d Weyl SOC. We find that as the SOC strength increases, the critical interaction strength leading to the FM state is dramatically reduced due to the nearly flat band structure near the bottom (Weyl shell) of the spectrum. We present a systematic symmetry classifications of the SOC Hamiltonian and establish their exact constraints on various density-spin correlation functions. We also analyze the symmetry breaking in the itinerant FM and the counting of the elementary excitations above the FM state. In the paramagnetic side, we identify one gapless sound mode

and three gapped modes. The SOC leads to the splitting of two transverse modes at any finite momentum. In the FM side, there are at least three main new features which are dramatically different than those without SOC: (a) The FM ground state acquires a non-zero momentum opposite to the direction of the magnetization, which can be detected by the absorption of images after Time of Flight (TOF) [4]. (b) Increasing the magnetization will drive a topological Lifshitz type of quantum phase transition (TQPT), which has experimentally detectable critical behaviors in density of states, specific heat, compressibility and spin susceptibility [18]. The nature of collective modes also changes dramatically across the TQPT. (c) Due to the locking of the spin and the non-zero momentum acquired by the FM ground state, the symmetry breaking leads to one gapped transverse pseudo-Goldstone mode instead of one gapless Goldstone mode. In view of the rapid technical development of cold atoms in Bragg spectroscopy [20, 21], speckling, tomographic, specific heat and *In-Situ* measurements [22–26], our theoretical predictions could be probed in near future experiments in both cold atoms and relevant condensed matter systems.

Path Integral formulation.— We consider a repulsively interacting two-component Fermi gas with the isotropic Weyl SOC $V_{SO} = \lambda \vec{k} \cdot \vec{\sigma}$, described by the Hamiltonian

$$H = \int d^3\vec{r} \Psi^\dagger \left(\frac{-\hbar^2 \nabla^2}{2m} - \mu + V_{SO} \right) \Psi + g \int d^3\vec{r} \Psi_\uparrow^\dagger(\vec{r}) \Psi_\downarrow^\dagger(\vec{r}) \Psi_\downarrow(\vec{r}) \Psi_\uparrow(\vec{r}), \quad (1)$$

where the SOC strength $\lambda = \frac{g_F \mu_B \nabla B}{3m\hbar}$ can be tuned by the magnetic field gradient ∇B in the scheme [6, 7], g_F the Landé factor and μ_B the Bohr magneton, $g = 4\pi\hbar^2 a_s / m$ with a_s the s -wave scattering length. The chemical po-

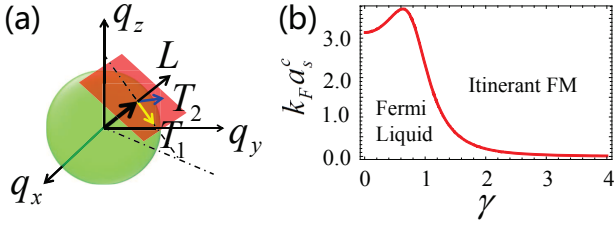


FIG. 1: (Color online) (a) The helicity basis: one longitudinal model L and two transverse modes T_1, T_2 . (b) Critical interaction strength $k_F a_s^c$ to the itinerant FM as a function of SOC strength $\gamma = k_R/k_F$.

tential μ is determined by the density of atoms self-consistently. We characterize the SOC strength by the dimensionless ratio $\gamma = k_R/k_F$ where $k_R = m\lambda$ and $k_F = \hbar(6\pi^2 n)^{1/3}$ is the Fermi momentum of the system without SOC at the same density n . In what follows, we will set $\hbar = 1$.

The interaction can be divided into the density and spin channel $\mathcal{H}_I = \frac{g}{8} \int d\vec{r} [\rho(\vec{r})^2 - \vec{S}(\vec{r})^2]$, where $\rho(\vec{r}) = \Psi^\dagger \Psi(\vec{r})$ and $\vec{S}(\vec{r}) = \Psi^\dagger \vec{\sigma} \Psi(\vec{r})$. In the presence of SOC, the density fluctuation is coupled with the spin fluctuation[11]. We introduce the density-spin order parameter $\phi_\mu, \mu = n, x, y, z$ to decouple the interaction term via a Hubbard-Stratonovich transformation. Integrating out the fermionic fields leads to the effective action for ϕ_μ :

$$\mathcal{S} = \int d^3\vec{r} \int_0^{1/T} d\tau \frac{1}{2g} \phi_\mu^2 - \text{Tr} \ln(-\mathcal{G}_0^{-1} + M), \quad (2)$$

where $\mathcal{G}_0^{-1} = -\partial_\tau - \mathcal{H}_0 + \mu$, $M = \frac{i}{2} \phi_n \sigma^0 + \frac{1}{2} \vec{\phi} \cdot \vec{\sigma}$.

The density channel ϕ_n has a non-zero imaginary saddle point value due to the finite particle density of the fermions which could be eliminated by re-defining ϕ_n as the deviation from its saddle point value. To the second order of ϕ_μ , we obtain: $\mathcal{S}_H^{(2)} = 1/(2\beta V) \sum_{\vec{q}, n} \mathcal{K}^{\mu\nu} \phi_\mu(-\vec{q}, -i\omega_n) \phi_\nu(\vec{q}, i\omega_n)$, where $\mathcal{K}^{\mu\nu} = \delta^{\mu\nu}/g - \bar{\chi}^{\mu\nu}(\vec{q}, i\omega_n)/4$, $\bar{\chi}^{\mu\nu}$ is related to the usual density-spin susceptibility $\chi^{\mu\nu}(\vec{q}, i\omega_n) = \langle s^\mu(\vec{q}, i\omega_n) s^\nu(-\vec{q}, -i\omega_n) \rangle$ via $\bar{\chi}^{00} = -\chi^{00}$, $\bar{\chi}^{0i} = i\chi^{0i}$, $\bar{\chi}^{ij} = \chi^{ij}$ with $i, j, = x, y, z$.

Symmetry analysis of the SOC Hamiltonian.— Before performing any analytical or numerical calculations, it is important to investigate the symmetry of the system and their implication on experimentally observable physical quantities. The symmetry analysis for interacting SOC systems is very different from any previously known (non)-relativistic systems and have never been systematically discussed before [9, 19]. Here, we classify the symmetries of the 3d Weyl SOC Hamiltonian Eqn. (1) and also find their exact constraints on various density-spin correlation functions. In the following section, we will

present the symmetry breaking patterns of the itinerant FM and the counting of the collective excitations above the FM phase.

For the Weyl SOC, the symmetries of the Hamiltonian Eqn. (1) are as follows: (i) continuous $[SU(2)_{spin} \times SO(3)_{orbit}]_D$, where the subscript D represents the simultaneous rotations in both spin and orbital space; (ii) the time reversal symmetry \mathcal{T} : $\mathcal{T}\Psi_{\vec{k}\uparrow}\mathcal{T}^{-1} = \Psi_{-\vec{k}\downarrow}$ and $\mathcal{T}\Psi_{\vec{k}\downarrow}\mathcal{T}^{-1} = -\Psi_{-\vec{k}\uparrow}$ which imply $\vec{S} \rightarrow -\vec{S}, \vec{k} \rightarrow -\vec{k}$; (iii) three spin-orbital coupled discrete symmetries: $\mathcal{P}_x = [\mathcal{I}_x \times \mathcal{S}_x]_D$ where $\mathcal{I}_x : p_x \rightarrow p_x, p_{y,z} \rightarrow -p_{y,z}$ the spatial reflection operator about x axes and $\mathcal{S}_x : s_x \rightarrow s_x, s_{y,z} \rightarrow -s_{y,z}$ a π rotation about S_x axes; similarly, there are another two discrete symmetries: $\mathcal{P}_y = [\mathcal{I}_y \times \mathcal{S}_y]_D$ and $\mathcal{P}_z = [\mathcal{I}_z \times \mathcal{S}_z]_D$. Note that the \mathcal{P}_z is just a special case of $[SU(2)_{spin} \times SO(3)_{orbit}]_D$ symmetry with a π rotation about S_z axes. These symmetries can be used to establish exact relations on the spin-density correlation functions, some of which are listed here, whose details are given in the SM [27].

In the presence of SOC, it is convenient to define a helical basis (Fig. 1 (a)) where we can define two transverse spin modes ($\hat{T}_1 \cdot \vec{S}, \hat{T}_2 \cdot \vec{S}$) and one longitudinal L spin mode ($\hat{q} \cdot \vec{S}$). The $[SU(2)_{spin} \times SO(3)_{orbit}]_D$ symmetry dictates that the dynamic 4×4 density-spin response function $\chi^{\mu\nu}(\vec{q}, \omega)$ can be split into two 2×2 subspaces: i) $n - L$ subspace ii) $T_1 - T_2$ subspace.

In the $T_1 - T_2$ subspace, after a unitary transformation, it can be shown that

$$\chi = \begin{pmatrix} \chi^{+-} & 0 \\ 0 & \chi^{-+} \end{pmatrix}, \quad \chi^{+-}(\vec{q}, \omega) = \chi^{-+}(-\vec{q}, \omega), \quad (3)$$

whose poles lead to two gapped transverse collective modes T^+, T^- respectively.

In the $n - L$ subspace,

$$\begin{aligned} \chi^{nn}(\vec{q}, \omega) &= \chi^{nn}(-\vec{q}, \omega), \quad \chi^{LL}(\vec{q}, \omega) = \chi^{LL}(-\vec{q}, \omega), \\ \chi^{nL}(\vec{q}, \omega) &= \chi^{Ln}(\vec{q}, \omega) = -\chi^{nL}(-\vec{q}, \omega). \end{aligned} \quad (4)$$

Diagonization in the $n - L$ space leads to a gapless sound mode and a gapped L mode.

These exact relations can be used to simplify considerably the following analytical and numerical calculations to find four collective modes. Any approximations such as random phase approximation (RPA) calculations in the next section should respect these exact relations.

Collective modes in the paramagnetic phase.— Adding density-spin sources to Eq. (2) and integrating out ϕ_μ , one can extract collective modes through the poles of density-spin response functions at the RPA level. We checked that they all satisfy the exact relations Eqn. (3) and (4). In the $n - L$ subspace, the mixing of density and longitudinal mode leads to one gapless sound mode $\omega_s = v_s q$ and one gapped (called L) mode $\omega_L(\vec{q}) = \Delta + \alpha q^2$ (Fig. 2 (a)). In the $T_1 - T_2$ subspace, there are two

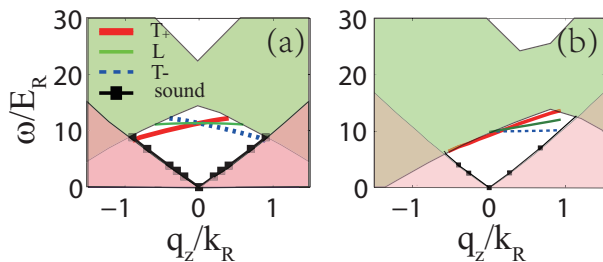


FIG. 2: (Color online) The collective modes of 3d Weyl SOC Fermi gas at $\gamma = 0.58$ (a) in the normal state $\zeta = 0$ and (b) in the weak FM state $\zeta = 1.5$. The pink (green) regime represents the intra-(inter) band particle-hole excitation.

split transverse modes $\omega_{T_{\pm}}(\vec{q}) = \Delta \pm \beta q$ (Fig. 2 (a)). The T_+ mode is the pole of χ^{+-} , while T_- is the pole of χ^{-+} . All the long wavelength behaviors of the four modes can be deduced through the symmetry constraint up to coefficients [27]. As shown in the SM, the split of the two transverse modes for finite \vec{q} is due to the absence of inversion symmetry (or equivalently \mathcal{S}_x or \mathcal{S}_y symmetry) of the Weyl SOC. The exact symmetry Eqn. (3) indicates that T_+ and T_- exchanges under $\vec{q} \rightarrow -\vec{q}$. The restored $SU(2)_{spin}$ symmetry at $\vec{q} = 0$ dictates that the three gapped modes must have the same gap Δ at $\vec{q} = 0$. We find Δ vanishes for interaction strength larger than $g_s = 24\pi^2 k_R/m(k_2^2 - k_1^2)$, where $k_2 > k_1$ are the two Fermi momenta in the presence of SOC. This corresponds to an instability driven by the collective modes.

Ferromagnetic instability.— There is also a FM instability when the static spin susceptibility diverges at $\delta = \frac{1}{g_c} - \frac{\chi_0}{4} = 0$, i.e., the Stoner instability. Here $\chi_0(\vec{q} \rightarrow 0, \omega = 0) = \frac{m}{6\pi^2} (\frac{k_1^2 + k_2^2}{K} + \frac{k_2^2 - k_1^2}{k_R})$, $K = \sqrt{k_R^2 + 2m\mu}$ is the static spin susceptibility of 3D non-interacting Fermi gas with the Weyl SOC. We obtain the critical value of dimensionless interaction strength $k_F a_s^c = F(\gamma)$ as shown in Fig. 1 (b). As γ increases, $F(\gamma)$ has a maximum at $\gamma \simeq 0.63$ corresponding to the chemical potential $\mu = -\frac{2}{3}E_R$, after which, $k_F a_s^c$ decreases quickly. At a strong SOC, the μ approaches the bottom of the spectrum (the Weyl shell at $|\vec{k}| = k_R$) where the density of states diverges as $\frac{1}{\sqrt{\epsilon}}$. The effects of an interaction are dramatically enhanced, even a weak interaction will drive the system into the itinerant FM state [29]. In a ${}^6\text{Li}$ system, the two hyperfine sublevels $|1/2, -1/2\rangle$ and $|1/2, 1/2\rangle$ can be chosen as two pseudo-spin $1/2$ states. With $N \sim 10^4$ ${}^6\text{Li}$ atoms inside an isotropic trap with a trap frequency $2\pi \times 10\text{Hz}$, and a typical magnetic field gradient strength $\nabla B = 0.09\text{G}/\mu\text{m}$ (within practical range [30]), we estimate the critical interaction strength as $k_F a_s^c \simeq 0.19$, which is order of magnitude smaller than the value π (Fig.1b at $\gamma = 0$) at the same density without the SOC [15, 16].

We note that there is always $g_c < g_s$, which indicates that the ferromagnetic instability happens before that driven by the instability of the collective modes.

Topological Lifshitz transition in the FM side.— For $g > g_c$, the system moves to the ferromagnetic side where the magnetization $\langle \vec{\phi} \rangle = -\frac{g}{2} \langle \vec{M} \rangle \neq 0$ can pick up any direction (such as z direction). We find $M \sim (g - g_c)^{1/2}$ from the self-consistent equation which has the same critical exponent as the traditional case. Then we can redefine $\phi_{T1}, \phi_{T2}, \phi_L$ with respect to the magnetization axes (Note that they are defined with respect to the momentum \vec{q} in the para-magnetic side Fig. 1 (a)). The $[SU(2)_{spin} \times O(3)_{orbit}]_D$ symmetry is reduced to the $[U^z(1)_{spin} \times U^z(1)_{orbit}]_D$ around the magnetization axes. The discrete symmetries $\mathcal{P}_{x,y}$ and time reversal symmetry \mathcal{T} are also broken. The symmetry breaking analysis and the exact constraints on the spin-density correlation functions in the FM are presented in the SM [27].

The fermionic spectrum as shown in Fig. 3 (a)-(c) is given by

$$\xi_{\vec{k},s} = k_{\perp}^2 + k_z^2 + 2s\sqrt{k_{\perp}^2 + (k_z - \zeta)^2}, \quad (5)$$

where $s = \pm, k_{\perp} = \sqrt{k_x^2 + k_y^2}$. We have taken the momentum unit $k_R = m\lambda$ and energy unit $E_R = k_R^2/2m$. The dimensionless value $\zeta = \frac{Mg}{4\lambda k_R}$ which denotes the strength of magnetization is the crossing point of the two helicity branches. The spectrum in Fig. 3 has a global minimum at $\vec{k} = -1\hat{e}_z$, independent of the value of ζ . The magnetization \vec{M} induces a Fermi surface shift along the $\vec{k} = -1\hat{e}_z$, which is a momentum-spin locking effect due to SOC. The spin polarization changes as shown by the arrows. It can be shown that the local density current vanishes due to the presence of the SOC. Nevertheless, this finite ground state momentum can be detected by absorption-imaging the atom cloud after time of flight (TOF), where both the trap potential and the SOC are tuned off. This provides a simple and efficient method to detect the FM phase.

For a given particle density with increasing ζ , one can divide the FM phase into two regimes shown in Fig. 3. In the weak FM regime $\zeta \ll 1$ (Fig.3a,3d), there are still 2 Fermi surfaces. As \vec{M} increases, there is a zero temperature Lifshitz like topological quantum phase transition (TQPT) where the 2 Fermi surfaces changes into one near $\zeta \sim 0.3$ (Fig.3b,3e). Scaling functions (obey ω/T scaling) near the TQPT in the density of states, specific heat, compressibility, Wilson ratio and spin-susceptibility can be derived along the lines presented in [18].

Collective modes in the FM side.— There are also corresponding changes of the collective modes across the TQPT. In the weak FM before the TQPT: $\zeta \ll 1$ (Fig.3a), due to the reduced symmetry $[U^z(1)_{spin} \times U^z(1)_{orbit}]_D$ and the broken of the $\mathcal{P}_{x,y}$ and \mathcal{T} symmetry in the FM side, the two main effects of the small magneti-

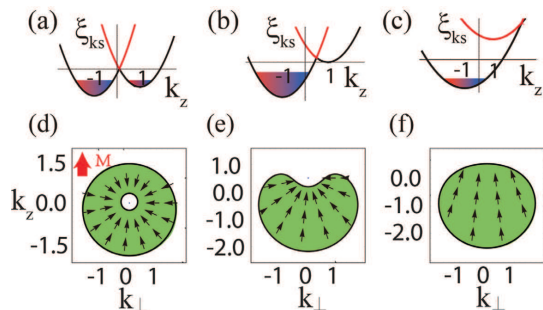


FIG. 3: (Color online) The topological quantum Lifshitz phase transition (TQPT) at the SOC strength $\gamma = 0.74$ tuned by the magnetization ζ where 2 Fermi surfaces changes into one near $\zeta \sim 0.3$. The fermionic spectrum $\xi_{\vec{k}s}$ (upper panel) and Fermi surfaces (down panel) at $\zeta = 0.1$ for (a),(d), $\zeta = 0.5$ for (b),(e), $\zeta = 3$ for (c),(f). The spectrum has a rotational symmetry about k_z axes. The black arrows show the spin polarization. The nature of collective modes also change across the TQPT (See Fig.2b and 4a,4b).

zation are (1) One gap in paramagnet side at $q = 0$ splits into three different gaps. The T_+ mode moves downward, while the T_- mode moves upward (Fig.2b). (2) The sound wave velocity[28] becomes anisotropic $\omega = v(\theta)q$ with only rotation symmetry around the \hat{z} axis, where $\cos \theta = \hat{q} \cdot \hat{M}$ [27]. All of these modes are still outside the particle-hole (PH) continuum, therefore remaining stable.

Across the TQPT, in the $n - L$ space, the mode coupling between the sound mode and the L mode becomes stronger, the sound mode starts to fall down into the intra-band PH continuum, while the L modes starts to merge up into the inter-band PH continuum. In the $T_1 - T_2$ space, the energy splits between T_+ and T_- mode also increases. Gradually, T_- mode merges up into the inter-band PH continuum and only T_+ survives the TQPT (Fig.4). The T_+ mode is, in fact, a gapped pseudo-Goldstone mode. Due to the locking of the spin and the non-zero momentum acquired by the FM ground state, the symmetry breaking $[SU(2)_{spin} \times O(3)_{orbit}]_D \rightarrow [U^z(1)_{spin} \times U^z(1)_{orbit}]_D$ only leads to gapped pseudo-Goldstone mode(s) instead of gapless Goldstone mode(s), in sharp contrast to the $SU(2)_{spin} \rightarrow U^z(1)_{spin}$ symmetry breaking in conventional Fermi systems without SOC (see the SM). Intuitively, one can view the non-zero momentum acquired by the FM ground state as an effective “external magnetic field” applied to a conventional FM without SOC, which opens a gap to the Goldstone mode. As shown in Fig.4a,4b, the pseudo-Goldstone mode develops a roton-like dispersion inside the intra-band P-H continuum, therefore unstable. As ζ increases, the roton minimum gets deeper and moves closer to $\vec{q} = 2\hat{e}_z$, which indicates possible short-ranged spin-density wave fluctuations inside the FM phase.

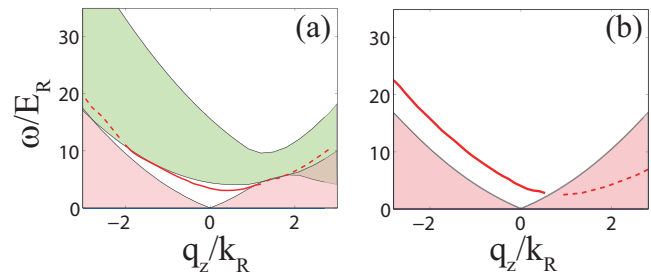


FIG. 4: (Color online) The evolution of the collective modes and particle-hole excitations at the SOC strength $\gamma = 0.74$ after the TQPT in Fig.3. $\zeta = 1.5$ for (a) and $\zeta = 20$ for (b). The pink (green) regime represents the intra- (inter-) band particle-hole continuum. As ζ increases, there is a large energy separation between the two helicities in Fig.3, the inter-band will move upward and out of (b) where only intra-band (pink) is drawn.

Discussions.— In Fermi systems without SOC, non-magnetic states with strong local correlations have been constructed to suppress the exchange energy [29]. These non-magnetic states may compete with the FM state. In the presence of SOC, it remains interesting to construct suitable non-magnetic states incorporating the short range correlations to compete with the FM state studied in this paper. We expect that the new mechanism and appealing physical picture discussed here to realize the itinerant FM may be robust against these possible non-magnetic states. However, different methods or approaches are needed to confirm or dispute the expectation. Unfortunately, the SOC makes the sign problem in the QMC much more serious than that without SOC. Spin density wave instability at $2k_R\hat{z}$ would be another serious competition. The itinerant FM can also display the anomalous Hall effect [31] and will be investigated in a future publication.

This work was supported by the NKBRFC under grants Nos. 2011CB921502, 2012CB821305, NSFC under grants Nos. 61227902, 61378017, 11434015, and SPRP-CAS under grants No. XDB01020300. J. Ye was supported by NSF-DMR-1161497, NSFC-11174210.

-
- [1] M. Z. Hasan and C. L. Kane, Rev. Mod. Phys. **82**, 3045 (2010).
 - [2] X. L. Qi and S. C. Zhang, Rev. Mod. Phys. **83**, 1057 (2011).
 - [3] For a review, see A. M. Turner and A. Vishwanath, arXiv:1301.0330.
 - [4] Y. J. Lin, K. Jiménez-García, and I. B. Spielman, Nature (London) **471**, 83 (2011); P. Wang, Z. Q. Yu, Z. Fu, J. Miao, L. Huang, S. Chai, H. Zhai, and J. Zhang, Phys. Rev. Lett. **109**, 095301 (2012); L. W. Cheuk, A. T. Som-

- mer, Z. Hadzibabic, T. Yefsah, W. S. Bakr, and M. W. Zwierlein, *Phys. Rev. Lett.* **109**, 095302 (2012).
- [5] For a review, see J. Dalibard, F. Gerbier, G. Juzeliūnas, and P. Öhberg, *Rev. Mod. Phys.* **83**, 1523 (2011).
- [6] Z.-F. Xu, L. You, and M. Ueda, *Phys. Rev. A* **87**, 063634 (2013).
- [7] B. M. Anderson, G. Juzeliūnas, V. M. Galitski, and I. B. Spielman, *Phys. Rev. Lett.* **108**, 235301 (2012).
- [8] Z. Q. Yu and H. Zhai, *Phys. Rev. Lett.* **107**, 195305 (2011); H. Hu, L. Jiang, X. -J. Liu, and H. Pu, *Phys. Rev. Lett.* **107**, 195304 (2011); C. Qu, Z. Zheng, M. Gong, Y. Xu, L. Mao, X. Zou, G. Guo, and C. Zhang, *Nat. Commun.* **4**, 2710 (2013); W. Zhang and W. Yi, *Nat. Commun.* **4**, 2711 (2013); J. P. Vyasankere and V. B. Shenoy, *Phys. Rev. B* **83**, 094515 (2011); J. P. Vyasankere, S. Zhang and V. B. Shenoy, *Phys. Rev. B* **84**, 014512 (2011); Qi Zhou and Xiaoling Cui, *Phys. Rev. Lett.* **110**, 140407.
- [9] Yu Yi-Xiang, Jinwu Ye and W.M. Liu, *Phys. Rev. A* **90**, 053603 (2014).
- [10] Y. Li and C. Wu, *Phys. Rev. B* **85**, 205126 (2012).
- [11] S. S. Zhang, X. L. Yu, J. Ye, and W. M. Liu, *Phys. Rev. A* **87**, 063623 (2013).
- [12] E. Stoner, *Philos. Mag.* **15**, 1018 (1933).
- [13] Y. Nagaoka, *Phys. Rev.* **147**, 392 (1966); A. Mielke, *J. Phys. A: Math. Gen.* **24**, L73 (1991); **24**, 3311 (1991); *Phys. Lett. A* **174**, 443 (1993); H. Tasaki, *Phys. Rev. Lett.* **69**, 1608 (1992); *Phys. Rev. B* **40**, 9192 (1989); *Commun. Math. Phys.* **242**, 445 (2003); A. Tanaka and H. Tasaki, *Phys. Rev. Lett.* **98**, 116402 (2007); Y. Li, E. H. Lieb, and C. Wu, *Phys. Rev. Lett.* **112**, 217201 (2014); H. Katsura and A. Tanaka, *Phys. Rev. A* **87**, 013617 (2013); L. Liu, H. Yao, Erez Berg, Steven R. White, and Steven A. Kivelson, *Phys. Rev. Lett.* **108**, 126406 (2012).
- [14] G. B. Jo, Y. R. Lee, J. H. Choi, C. A. Christensen, T. H. Kim, J. H. Thywissen, D. E. Pritchard, and W. Ketterle, *Science* **325**, 1521 (2009).
- [15] R. A. Duine and A. H. MacDonald, *Phys. Rev. Lett.* **95**, 230403 (2005); V. B. Shenoy and T.-L. Ho, *Phys. Rev. Lett.* **107**, 210401 (2011); D. Pekker, M. Babadi, R. Sensarma, N. Zinner, L. Pollet, M. W. Zwierlein, and E. Demler, *Phys. Rev. Lett.* **106**, 050402 (2011); S. Pilati, G. Bertaino, S. Giorgini, and M. Troyer, *Phys. Rev. Lett.* **105**, 030405 (2010); X. Cui and T.-L. Ho, *Phys. Rev. Lett.* **110**, 165302 (2013); *Phys. Rev. A* **89**, 023611 (2014).
- [16] J. A. Hertz, *Phys. Rev. B* **14**, 1165 (1976).
- [17] A. J. Millis, *Phys. Rev. B* **48**, 7183 (1993); U. Zülicke and A. J. Millis, *Phys. Rev. B* **51**, 8996 (1995).
- [18] F. -D. Sun, X. -L. Yu, J. Ye, H. Fan, W. M. Liu, *Scientific Reports* **3**, 2119 (2013).
- [19] Fadi Sun, Jinwu Ye, Wu-Ming Liu, arXiv:1408.3399.
- [20] M. Kozuma *et al.*, *Phys. Rev. Lett.* **82**, 871 (1999); J. Stenger *et al.*, *ibid.* **82**, 4569 (1999); D. M. Stamper-Kurn *et al.*, *ibid.* **83**, 2876 (1999); J. Steinhauer, R. Ozeri, N. Katz, and N. Davidson, *ibid.* **88**, 120407 (2002); S. B. Papp *et al.*, *ibid.* **101**, 135301 (2008); P. T. Ernst *et al.*, *Nature Phys.* **6**, 56 (2010).
- [21] Jinwu Ye, *et. al*, *Phys. Rev. A* **83**, 051604 (R) (2011); *Ann. Phys.* **328** (2013), 103-138.
- [22] C. Sanner, E. J. Su, A. Keshet, W. Huang, J. Gillen, R. Gommers, and W. Ketterle, *Phys. Rev. Lett.* **106**, 010402 (2011).
- [23] C. Sanner, E. J. Su, W. Huang, A. Keshet, J. Gillen, and W. Ketterle, *Phys. Rev. Lett.* **108**, 240404 (2012).
- [24] Y. Shin, C. H. Schunck, A. Schirotzek, and W. Ketterle, *Nature (London)* **451**, 689 (2008).
- [25] N. Gemelke, X. Zhang, C. -L. Huang, and C. Chin, *Nature (London)* **460**, 995 (2009).
- [26] J. Kinast, *et.al*, *Science* **25**, 1296-1299 (2005); M. J. H. Ku, *et.al*, *Science* **335**, 563-567 (2012).
- [27] See the Supplementary Materials for this manuscript.
- [28] It is important to stress that this gapless sound mode is not a Goldstone mode.
- [29] For example, see M. C. Gutzwiller, *Phys. Rev. Lett.* **10**, 159 (1963); *Phys. Rev.* **137**, A1726 (1965); J. Kanamori, *Prog. Theor. Phys.* **30**, 275 (1963). Y. M. Vilk, L. Chen, and A.-M. S. Tremblay, *Phys. Rev. B* **49**, 13267 (1994); Hui Zhai, *Phys. Rev. A* **80**, 051605 (R) (2009). For a review, see A. Auerbach, *Interacting electrons and quantum magnetism*, Springer-Verlag (1998).
- [30] M. Trinker, S. Groth, S. Haslinger, S. Manz, T. Betz, S. Schneider, I. Bar-Joseph, T. Schumm, and J. Schmiedmayer, *Appl. Phys. Lett.* **92**, 254102 (2008).
- [31] J. Ye, Y. B. Kim, A. J. Millis, B. I. Shraiman, P. Majumdar, and Z. Tešanović, *Phys. Rev. Lett.* **83**, 3737 (1999).

Supplementary Material for “Itinerant ferromagnetism of repulsive spin-orbit coupled Fermi gas”

Shang-Shun Zhang^{1,2}, Jinwu Ye^{2,3}, and Wu-Ming Liu¹

¹Beijing National Laboratory for Condensed Matter Physics,

Institute of Physics, Chinese Academy of Sciences, Beijing 100190, China

² Department of Physics and Astronomy, Mississippi State University, MS 39762, USA

³ Key Laboratory of Terahertz Optoelectronics, Ministry of Education,
Department of Physics, Capital Normal University, Beijing 100048, China

(Dated: April 24, 2019)

In this Supplementary material, in section I, we will first classify the symmetries of the Hamiltonian with a Weyl spin-orbit coupling (SOC) in Eqn. (M1) (we use M to stand for the figures and equations in the main text here and after) and also find their exact constraints on various density-spin correlation functions. We will also present the symmetry breaking patterns of the itinerant FM and the counting of the collective excitations above the FM phase. In Sec.II, we compute the collective modes through the poles of density-spin response functions at the random phase approximation (RPA) level and also check against the exact relations established in the Sec.I. For a constructive comparison, we also evaluate the collective modes inside the itinerant FM state of a conventional system without SOC.

I. SYMMETRY ANALYSIS OF WEYL SOC HAMILTONIAN

The Hamiltonian with a Weyl SOC in Eqn. (M1) has the following symmetries.

1. a combined rotational symmetry $[SU(2)_{spin} \times SO(3)_{orbit}]_D$
2. Time reversal symmetry \mathcal{T} : $\mathcal{T}c_{\vec{k},\uparrow}\mathcal{T}^{-1} = c_{-\vec{k},\downarrow}$, $\mathcal{T}c_{\vec{k},\downarrow}\mathcal{T}^{-1} = -c_{-\vec{k},\uparrow}$.
3. Three spin-orbital coupled reflection symmetries:
 - (a) $\mathcal{P}_x = [\mathcal{I}_x \times \mathcal{S}_x]_D$ with $\mathcal{I}_x : p_x \rightarrow p_x, p_{y,z} \rightarrow -p_{y,z}$ and $\mathcal{S}_x : s_x \rightarrow s_x, s_{y,z} \rightarrow -s_{y,z}$.
 - (b) $\mathcal{P}_y = [\mathcal{I}_y \times \mathcal{S}_y]_D$ with $\mathcal{I}_y : p_y \rightarrow p_y, p_{x,z} \rightarrow -p_{x,z}$ and $\mathcal{S}_y : s_y \rightarrow s_y, s_{x,z} \rightarrow -s_{x,z}$.
 - (c) $\mathcal{P}_z = [\mathcal{I}_z \times \mathcal{S}_z]_D$ with $\mathcal{I}_z : p_z \rightarrow p_z, p_{x,y} \rightarrow -p_{x,y}$ and $\mathcal{S}_z : s_z \rightarrow s_z, s_{x,y} \rightarrow -s_{x,y}$.

Note that the \mathcal{P}_z symmetry is also equivalent to a joint π rotation of orbital and spin around \hat{z} axis. so it is not a new symmetry. The \mathcal{P}_y can also be taken as \mathcal{P}_x combined with $[U(1)_{spin} \times U(1)_{orbit}]_D$ by an angle $\pi/2$.

A. Symmetry analysis in the para-magnet side

Without loss of generality, we can pick up \vec{q} as the \hat{z} axis, i.e., $\vec{q} = q_z \hat{z}$. Then, the helical basis shown in Fig. M1 (a) is just given by $\hat{T}_1 = \hat{x}, \hat{T}_2 = \hat{y}$ and $\hat{L} = \hat{z}$. The $[SU(2)_{spin} \times SO(3)_{orbit}]_D$ symmetry along this \hat{z} axis dictates that

$$R_z^T \chi^{\mu\nu} R_z = \chi^{\mu\nu}. \quad (S1)$$

Expanding it leads to the fact that the dynamical 4×4 density-spin response function $\chi^{\mu\nu}(\vec{q}, \omega)$ can be split into two 2×2 subspaces: i) $n - L$ subspace ii) $T_1 - T_2$ subspace with $\chi^{xx} = \chi^{yy}, \chi^{xy} = -\chi^{yx}$.

(1) In the $T_1 - T_2$ subspace

After a unitary transformation, it can be shown that in the $T_1 - T_2$ subspace:

$$\chi = \begin{pmatrix} \chi^{+-} & 0 \\ 0 & \chi^{-+} \end{pmatrix}, \quad (S2)$$

where $\chi^{+-} = 2(\chi^{xx} - i\chi^{xy}), \chi^{-+} = 2(\chi^{xx} + i\chi^{xy})$.

The \mathcal{P}_x (or \mathcal{P}_y) symmetry dictates

$$\chi^{+-}(\vec{q}, \omega) = \chi^{-+}(-\vec{q}, \omega). \quad (S3)$$

The \mathcal{T} symmetry leads to

$$\chi^{+-}(\vec{q}, \omega) = \chi^{-+}(-\vec{q}, \omega), \quad (S4)$$

which is identical to Eqn. (S3). This constraint leads to that $\chi^{xx} = \chi^{yy}$ is an even function of q_z , $\chi^{xy} = -\chi^{yx}$ is an odd function of q_z .

Directly taking complex conjugation of χ^\pm leads to:

$$[\chi^{+-}(\vec{q}, \omega)]^* = \chi^{-+}(-\vec{q}, -\omega), \quad (\text{S5})$$

which, combining with Eqn. (S3), leads to

$$\begin{aligned} \text{Re}\chi^{+-}(\vec{q}, \omega) &= \text{Re}\chi^{+-}(\vec{q}, -\omega), \\ \text{Im}\chi^{+-}(\vec{q}, \omega) &= -\text{Im}\chi^{+-}(\vec{q}, -\omega). \end{aligned} \quad (\text{S6})$$

Requiring $\chi^{\mu\nu}(\vec{q}, \omega)$ to be Hermite leads to that χ^{+-}, χ^{-+} are real, therefore, Eqn. (S6) gives rise to the fact that $\chi^{xx} = \chi^{yy}$ and $\chi^{xy} = -\chi^{yx}$ are all even function of ω . The poles of χ^{+-} and χ^{-+} lead to the two gapped transverse modes T_\pm respectively. In principle, χ^{+-}, χ^{-+} might also develop imaginary parts, i.e., $\text{Im}\chi^{+-}(\vec{q}, \omega) \neq 0$, which represents the damping of the collective modes. At RPA level as presented in the next section, the damping is due to the coupling with the particle-hole (P-H) excitations and the regime where $\text{Im}\chi^{+-}(\vec{q}, \omega) \neq 0$ is given by the P-H continuum as shown by the shaded regime in Fig. 1.

(2) In the $n - L$ subspace

The \mathcal{P}_x (or \mathcal{P}_y) symmetry dictates

$$\begin{aligned} \chi^{nn}(\vec{q}, \omega) &= \chi^{nn}(-\vec{q}, \omega), \chi^{LL}(\vec{q}, \omega) = \chi^{LL}(-\vec{q}, \omega), \\ \chi^{nL}(\vec{q}, \omega) &= -\chi^{nL}(-\vec{q}, \omega), \chi^{Ln}(\vec{q}, \omega) = -\chi^{Ln}(-\vec{q}, \omega), \end{aligned} \quad (\text{S7})$$

which shows χ^{nn}, χ^{LL} are even function of q_z , while χ^{nL}, χ^{Ln} are an odd function of q_z .

The \mathcal{T} symmetry leads to

$$\begin{aligned} \chi^{nn}(\vec{q}, \omega) &= \chi^{nn}(-\vec{q}, \omega), \chi^{LL}(\vec{q}, \omega) = \chi^{LL}(-\vec{q}, \omega), \\ \chi^{nL}(\vec{q}, \omega) &= -\chi^{Ln}(-\vec{q}, \omega), \chi^{Ln}(\vec{q}, \omega) = -\chi^{nL}(-\vec{q}, \omega). \end{aligned} \quad (\text{S8})$$

Note that \mathcal{P}_x and \mathcal{T} leads to two different equations in the nL component only. Combining Eqn. (S7) and Eqn. (S8) leads to $\chi^{nL}(\vec{q}, \omega) = \chi^{Ln}(\vec{q}, \omega)$.

Directly taking complex conjugation of χ^{ij} leads to:

$$[\chi^{ij}(\vec{q}, \omega)]^* = \chi^{ij}(-\vec{q}, -\omega), \quad i, j = n, L, \quad (\text{S9})$$

which combining with Eqn. (S7) leads to

$$\begin{aligned} \text{Re}\chi^{ii}(\vec{q}, \omega) &= \text{Re}\chi^{ii}(\vec{q}, -\omega), \quad i = n, L, \\ \text{Im}\chi^{ii}(\vec{q}, \omega) &= -\text{Im}\chi^{ii}(\vec{q}, -\omega), \end{aligned} \quad (\text{S10})$$

and

$$\begin{aligned} \text{Re}\chi^{nL}(\vec{q}, \omega) &= -\text{Re}\chi^{nL}(\vec{q}, -\omega), \\ \text{Im}\chi^{nL}(\vec{q}, \omega) &= \text{Im}\chi^{nL}(\vec{q}, -\omega). \end{aligned} \quad (\text{S11})$$

Requiring $\chi^{\mu\nu}(\vec{q}, \omega)$ to be Hermite leads to that $\chi^{nn}, \chi^{LL}, \chi^{nL}$ are real. Based on Eqn. (S10) and (S11), we know that $\chi^{nn}(\vec{q}, \omega), \chi^{LL}(\vec{q}, \omega)$ are even function of ω , while $\chi^{nL}(\vec{q}, \omega)$ is an odd function of ω . Similarly, $\chi^{nn}, \chi^{LL}, \chi^{nL}$ might also develop imaginary parts: $\text{Im}\chi^{ij}(\vec{q}, \omega) \neq 0, i, j = n, L$, which represents the damping of collective modes. In principle, the damping of the collective modes in the (T_1, T_2) sector needs not to happen at the same time as that in the (n, L) sector. However, at the RPA level (see Eqn. (S16)), both of them are damped through the P-H excitations and therefore they happen at the same time.

These exact relations lead to strong constraints on the behaviors of the collective modes without any approximations. For example, the restored $SU(2)_{spin}$ symmetry at $\vec{q} = 0$ dictates that the three gapped modes found here must have the same gap Δ at $\vec{q} = 0$. Then, one can expand the pole equation $\det[\chi^{-1}(\vec{q}, \omega)] = 0$ near the gap $(\vec{q}, \omega) = (\vec{0}, \Delta)$ by using the above symmetry constraints on the $\chi^{\mu\nu}$ to obtain the dispersions of the gapped modes. In the (T_1, T_2) subspace, we find there must be two split transverse modes T_\pm (Fig. 1): $\omega_{T_\pm} = \Delta \pm \beta q + \mathcal{O}(q^2)$. The mixing of density and longitudinal mode in the (n, L) subspace leads to one gapless sound mode $\omega_q^s = v_s q + \mathcal{O}(q^2)$ and one gapped (called L) mode $\omega_L(\vec{q}) = \Delta + \alpha q^2 + \mathcal{O}(q^3)$ (Fig. 1).

(3) The symmetry reason why T_+ and T_- split at finite \vec{q} .

In the following, we show that in order to guarantee the two T_+, T_- modes to be degenerate, one need to have both \mathcal{T} symmetry and the inversion symmetry $\mathcal{I}: \vec{q} \rightarrow -\vec{q}$. The \mathcal{I} symmetry dictates that

$$\chi^{+-}(\vec{q}, \omega) = \chi^{+-}(-\vec{q}, \omega), \chi^{-+}(\vec{q}, \omega) = \chi^{-+}(-\vec{q}, \omega). \quad (\text{S12})$$

Combining Eqn. (S4) with Eqn. (S12) lead to:

$$\chi^{+-}(\vec{q}, \omega) = \chi^{-+}(\vec{q}, \omega). \quad (\text{S13})$$

However, it is the SOC which breaks the inversion symmetry at $\vec{q} \neq 0$, therefore, $\chi^{+-}(\vec{q}, \omega) \neq \chi^{-+}(\vec{q}, \omega)$ for $\vec{q} \neq 0$. This leads to the splitting of the two transverse modes even in the normal phase at any $\vec{q} \neq 0$. Only at $\vec{q} = 0$, the inversion symmetry is restored, and the three modes have the same gaps.

Alternatively, if assuming S_x symmetry: $\sigma_x \rightarrow \sigma_x, \sigma_{y,z} \rightarrow -\sigma_{y,z}$, one also find Eqn. (S13) which leads to the degeneration of the two transverse modes. In the presence of SOC, only \mathcal{S}_x symmetry combined with the reflection symmetry $\mathcal{I}_x: q_x \rightarrow q_x, q_{y,z} \rightarrow -q_{y,z}$, i.e., the \mathcal{P}_x symmetry, is preserved in general. Therefore, the two transverse modes T_{\pm} are non-degenerate for any non-zero \vec{q} . Exception happens at $\vec{q} = 0$ where the \mathcal{S}_x symmetry is restored, which leads to the degeneration of the energy gaps.

B. Symmetry breaking analysis in the FM side

In the FM side, if choosing the symmetry breaking direction along \hat{z} without loss of generality, the $[SU(2)_{spin} \times SO(3)_{orbit}]_D$ symmetry is reduced to $[U^z(1)_{spin} \times U^z(1)_{orbit}]_D$. If choosing \vec{q} along the magnetization direction $\vec{q} = q_z \hat{z}$, the dynamical 4×4 density-spin response functions $\chi^{\mu\nu}(q_z, \omega)$ can still be split into two 2×2 subspaces: i) $n - L$ subspace ii) $T_1 - T_2$ subspace with $\chi^{xx} = \chi^{yy}, \chi^{xy} = -\chi^{yx}$. Then, in the $T_1 - T_2$ subspace, Eqn. (S2) follows. However, there are no \mathcal{T} and $\mathcal{P}_x, \mathcal{P}_y$ symmetry anymore. Even the \mathcal{S}_x symmetry at $\vec{q} = 0$ is broken due to the spin polarization. As analyzed above, the degeneration of the two transverse gapped modes at $\vec{q} = 0$ is lifted. Furthermore, due to the loss of the $SU(2)_{spin}$ symmetry at $\vec{q} = 0$, the degeneration of the three gapped modes is lifted.

For a general $\vec{q} = (q_z, \vec{q}_{\perp})$, the invariance under the $[U^z(1)_{spin} \times U^z(1)_{orbit}]_D$ rotation leads to:

$$\chi_{n,L,T_1,T_2}(q_z, \vec{q}_{\perp}, \omega) = \chi_{n,L,T'_1,T'_2}(q_z, U\vec{q}_{\perp}, \omega), \quad (\text{S14})$$

where $(T'_1, T'_2) = U(T_1, T_2)$ stands for the $U^z(1)_{spin}$ rotation on the two transverse axis of the helicity basis, while the $U\vec{q}_{\perp}$ in the Eqn. (S14) stands for the $U^z(1)_{orbit}$ rotation on orbital vectors. Eqn. (S14) immediately imply $\chi_{n,L,T_1,T_2}(q_z, \vec{q}_{\perp}, \omega)$ is a function of (q_z, q_{\perp}, ω) only. As a result, the collective modes are rotational symmetric around the magnetization axes (\hat{z} axes as assumed here). For example, the sound mode $\omega_s = v_s(q_z, q_{\perp})q = v_s(\theta)q$ where $\tan \theta = q_z/q_{\perp}$. Setting $q_{\perp} = 0$, Eqn. (S14) reduces to $\chi_{n,L,T_1,T_2}(q_z, \omega) = \chi_{n,L,T'_1,T'_2}(q_z, \omega)$ which lead to the $4 \rightarrow 2 + 2$ decomposition mentioned above. However, in the $q_{\perp} \neq 0$ case, there is no such decomposition anymore, all the 4 modes are mixed, so there is no distinctions of n, L, T_1, T_2 modes anymore.

II. COLLECTIVE MODES AND P-H EXCITATIONS FOR 3D FERMI GAS WITH AND WITHOUT SOC AT THE RPA LEVEL

In the last section, we established all the possible exact relations on the density-spin response functions from the general symmetry principle. Any analytical approximations or numerical calculations must satisfy these exact relations. In this section, we will perform a concrete calculation on all the response functions at the RPA level whose poles lead to the collective modes. We also checked that they all satisfy the exact relations.

Now we can expand Eqn.M2 $\mathcal{S}[\phi_{\mu}] = \mathcal{S}^{(0)} + \mathcal{S}^{(2)} + \dots$ in terms of ϕ_{μ} . As said in the main text, the density channel ϕ_n has a non-zero imaginary saddle point value due to the finite particle density of the fermions which could be eliminated by re-defining ϕ_n as the deviation from its saddle point value. To the second order of ϕ_{μ} , we obtain

$$\mathcal{S}^{(2)} = \frac{1}{2} \int \frac{d^3\vec{k}}{(2\pi)^3} T \sum_n \left(\frac{1}{g} \delta^{\mu\nu} - \frac{1}{4} \bar{\chi}^{\mu\nu}(\vec{k}, i\omega_n) \right) \phi^{\mu}(\vec{k}, i\omega_n) \phi^{\nu}(-\vec{k}, -i\omega_n), \quad (\text{S15})$$

where $\bar{\chi}^{\mu\nu}$ is related to the density-spin susceptibility $\chi^{\mu\nu}(\mathbf{q}, i\omega_n) = \langle s^{\mu}(\mathbf{q}, i\omega_n) s^{\nu}(-\mathbf{q}, -i\omega_n) \rangle$ via $\bar{\chi}^{00} = -\chi^{00}$,

$\bar{\chi}^{0i} = i\chi^{0i}$, $\bar{\chi}^{i0} = i\chi^{i0}$, $\bar{\chi}^{ij} = \chi^{ij}$ with $i, j = x, y, z$. The non-interacting density-spin susceptibility is given by:

$$\chi_0^{\mu\nu}(\vec{q}, i\omega_n) = \frac{1}{V} \sum_{k, sr} F_{sr}^{\mu\nu}(k+q, k) \frac{n_F(\xi_{k+q,s}) - n_F(\xi_{k,r})}{i\omega_n - (\xi_{k+q,s} - \xi_{k,r})}, \quad (\text{S16})$$

where the $\xi_{k,s}$ is the fermion spectrum with s the helicity $\hat{p} \cdot \vec{\sigma}|ps\rangle = s|ps\rangle$, the $n_F(\xi_{k,s})$ is the Fermi distribution function, the $\xi_{k+q,s} - \xi_{k,r}$ is the particle-hole excitation energy and the overlap factor $F_{sr}^{\mu\nu}(p, q) = \langle ps|\sigma^\mu|qr\rangle\langle qr|\sigma^\nu|ps\rangle$.

A. Collective modes for 3D Fermi gas with SOC in the normal side

As shown in the Sect.I, the $[SU(2)_{spin} \times SO(3)_{orbit}]_D$ symmetry^{1,2} dictates that the dynamical 4×4 density-spin susceptibility Eqn. (S16) can be split into two 2×2 subspaces: i) $n-L$ subspace formed by the density and the longitudinal spin mode ii) $T_1 - T_2$ subspace formed by the two transverse modes. This exact decomposition simplifies the following analytical and numerical calculations considerably.

The gapless sound mode in the $n-L$ subspace, $\omega_s = v_s q$ in Fig. 1 is determined by the pole of 2×2 density-spin susceptibility: $\det(1 + \frac{g}{4}\sigma_z\chi_{nL}) = 0$ with

$$\chi_0^{nL}(\vec{q}, \omega) = \frac{m(k_1^2 + k_2^2)}{2\pi^2\kappa} \begin{pmatrix} F(y) & \beta y F(y) \\ \beta y F(y) & \frac{1}{3} + \frac{\sqrt{k_R^2 + 2m\mu}}{3k_R} \beta + y^2 F(y) \end{pmatrix}, q \rightarrow 0 \text{ with } \omega/v_F q \text{ fixed}, \quad (\text{S17})$$

where $k_2 > k_1$ are the two Fermi momenta in Fig. 3 (a), $2\kappa = k_1 + k_2$ ($k_2 - k_1$) for $\mu > 0$ ($\mu < 0$), $\beta = \frac{k_2^2 - k_1^2}{k_2^2 + k_1^2}$ and $y = \omega/v_F q$, v_F the Fermi velocity, $F(y) = 1 + \frac{y}{2} \ln \frac{y+1}{y-1}$. It is easy to see that Eqn. (S17) indeed satisfies the constraints Eqn. (S10) and (S11). We numerically determined the velocity v_s of this gapless sound mode at different μ/E_R as shown in Fig. 3 (b). This sound mode corresponds to a coupled density-longitudinal spin fluctuation.

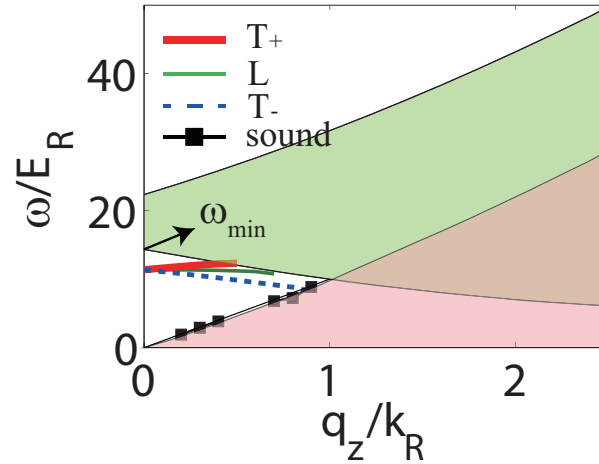


FIG. 1: (Color online) Collective modes for 3D Fermi gas with Weyl type SOC in the normal side. The parameter here are: $\mu/E_R = 20$ (equivalent to SOC strength $\gamma = 0.58$) which corresponds to the case iii in Fig. 3 and $a_s = 0.9a_s^c$. The green (yellow) region is the intra-band (inter-band) particle-hole excitation continuum. ω_{min} denotes the lower edge of inter-band particle-hole excitation continuum, which is taken as the unit in Fig. 3 (d). In fact, this figure is re-drawing of Fig.M2a in the helicity basis. Namely, folding Fig.M2a left $q_z < 0$ back to the right $q_z > 0$ and changing the q_z axis to the q axis lead to this figure shown here. Alternatively, picking \vec{q} along the \hat{z} axis and inverting with respect to the origin gives back to Fig.M2a.

At the RPA level, from Eqn. (S2), the two transverse modes are determined by

$$1 - \frac{g}{2}\chi_0^{+-}(\vec{q}, \omega) = 0, \quad 1 - \frac{g}{2}\chi_0^{-+}(\vec{q}, \omega) = 0, \quad (\text{S18})$$

where $\chi_0^{+-}(\vec{q}, \omega) = 2(\chi^{xx} - i\chi^{xy})$ is given by Eqn. (S16). Eqn. (S18) leads to the T_{\pm} mode in Fig. 1.

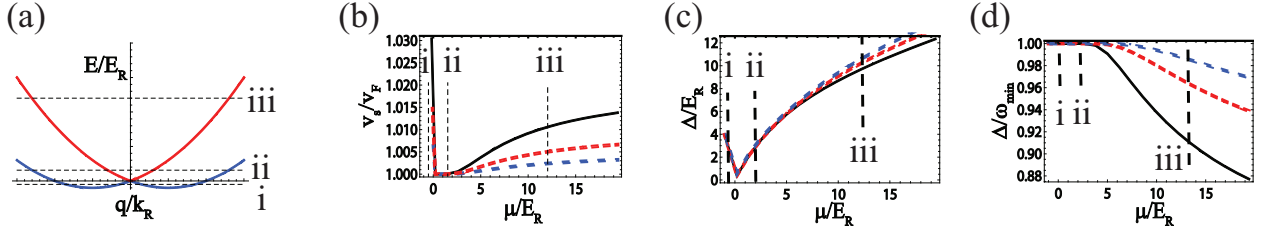


FIG. 2: (Color online) (a) Single particle energy spectrum of SOC Fermi gas in the normal state. Shown are different filling cases by the dashed lines i, ii and iii. (b) ratio v_s/v_F of gapless sound mode (c) δ/E_R and (d) δ/ω_{min} show the energy gap for the three gapped modes. The unit ω_{min} is shown in Fig. 1. The three different colors represent different interaction strengths, i.e., Black (critical interaction strength g_c for ferromagnetic phase transition), Red dashed ($g = 4/5g_c$), Blue dotted ($g = 2/3g_c$).

In all, there are three branches of gapped mode, one L mode within the $n-L$ subspace and the other two T_{\pm} modes within the $T_1 - T_2$ subspace. Due to the $SU(2)_{spin}$ symmetry at $\vec{q} = 0$, the three gapped modes are degenerate at $\vec{q} = 0$ where the gap is determined by $\det[1 - \frac{q}{4}\chi_{spin}(\omega, \vec{q} = 0)] = 0$, with

$$\chi_{spin}^{ij}(\omega, \vec{q} = 0) = \frac{m}{6\pi^2 k_R} \left(k_2^2 - k_1^2 + \frac{m^2 \omega^2}{4k_R^2} \ln \left[\frac{4k_R^2 k_2^2 - m^2 \omega^2}{4k_R^2 k_1^2 - m^2 \omega^2} \right] \right) \delta^{ij}, i, j = x, y, z, \quad (S19)$$

The numerical result of this energy gap Δ at different μ/E_R is shown in Fig. 3 (c) (in units of the recoil energy $E_R = k_R^2/2m$) and Fig. 3 (d) (in units of the lower edge of inter-band particle-hole excitation energy ω_{min} shown in Fig. 1).

In Fig. 3 (a), we plot three typical filling cases shown by the dashed lines: i) dilute density case with $\mu < 0$; ii) $\mu > 0$ but close to the Dirac point ($\mu = 0$), iii) dense density case. Fig. 1 belongs to the case iii. In Fig. 3 (b), as the filling tends to the Dirac point from above $\mu > 0$, the v_s/v_F decreases close to 1. Pass the Dirac point, the ratio increases quickly. In Fig. 3 (c), the Δ/E_R decreases close to zero (At the Dirac point, the blank regime between the inter-band and intra-band particle-hole excitation shown in Fig. 1 shrinks to zero). Pass the Dirac point, the ratio increases also. To show the relationship between the energy gap Δ and the P-H excitation, in Fig. 3 (d) we show Δ/ω_{min} with ω_{min} the lower edge of the inter-band particle-hole excitation energy shown in Fig. 1. We find as the chemical potential decreases from iii to i, the ratios gets to 1 from below, namely, the gapped collective modes move more closer to the edge of inter-band particle-hole excitation continuum in Fig. 1. In the dilute limit $\mu \rightarrow -1$, the critical interaction strength to get to FM $g_c = 12\pi^2 \sqrt{1 + \mu} + \mathcal{O}((1 + \mu)^{3/2})$ reduces to zero, the sound velocity saturates at $v_s/v_F \simeq 1.102$, the energy gap increases and moves close to the P-H continuum $\Delta_s/E_R \simeq 4(1 - \sqrt{1 + \mu})$.

The level repulsion in the $n-L$ space will push the sound mode quite close to the intra-band P-H continuum (Fig. 1,2). Similarly, the level repulsion in the T_1, T_2 space will also split the two transverse modes T_{\pm} . So at finite, but small q , the three modes split with $\omega_{T_+} > \omega_L > \omega_{T_-}$.

B. Collective modes across the ferromagnetic phase transition without SOC

As a comparison, it is instructive to perform a detailed calculation on the collective mode in the conventional system without SOC. To the best of the authors knowledge, there are no previous literatures to discuss this important and tricky physical picture.

In the normal side, due to the $SU(2)_{spin} \times SO(3)_{orbit}$ symmetry, the density and spin are decoupled, the density and spin susceptibility are $\chi^{\mu\nu} = \chi_0 \delta^{\mu\nu}$ where $\mu, \nu = n, s_x, s_y, s_z$. Since the interaction is repulsive (attractive) in the density (spin) channel, there is only one gapless density mode with linear dispersion $\omega_q = v_s q$, i.e., zero sound in the density channel, no stable collective modes in the spin channel (Fig. 3 (a)).

In the FM side, there is a spin polarization \vec{M} (for example, along \hat{z}), and the symmetry breaking pattern is $SU(2)_{spin} \rightarrow U(1)_z$. The presence of the magnetic order suddenly changes the structure of the fermion propagator and also the density and spin susceptibility. This is in sharp contrast to the SOC system presented above and the main text. In concrete, the fermion propagator takes the form:

$$\mathcal{G}(i\omega_n, \vec{k}) = \frac{1}{2} \sum_{s=\pm 1} \frac{\sigma_0 + s\sigma_z}{i\omega_n - \vec{k}^2/2m + sgM/4}. \quad (S20)$$

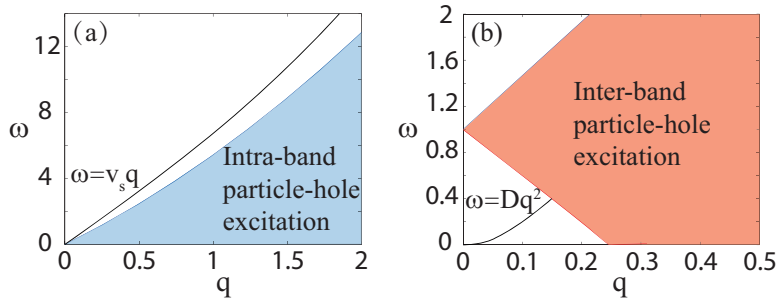


FIG. 3: (Color online) The particle-hole continuum and collective modes in traditional Fermi gas: (a) zero sound in the normal side and (b) quadratic spin mode in the FM side.

As said above, the remaining symmetry $U(1)_z$ dictates that the density-spin susceptibility $\chi^{\mu\nu}$, $\mu, \nu = n, s_x, s_y, s_z$ can be decoupled to two 2×2 matrixes: one for the density and longitudinal spin mode $\hat{L} = \vec{M}/M$, another for the two transverse spin modes $\hat{T}_1 \cdot \vec{M} = \hat{T}_2 \cdot \vec{M} = 0$. In the density-longitudinal subspace, the density fluctuation is strongly coupled with the longitudinal spin fluctuation, the 2×2 susceptibility takes the form:

$$\chi^{(nL)} = \chi_0 \begin{pmatrix} 1 & -1 \\ -1 & 1 \end{pmatrix}, \quad (\text{S21})$$

where $\chi_0 = \frac{mk_F^2}{4\pi^2} (2 + y \ln \frac{y-1}{y+1})$ with $y = m\omega/k_F q$. Due to the absence of any poles in $\det[1 + \frac{q}{4}\sigma_z \chi^{nL}] = 0$, there are no collective modes in the $n - L$ subspace. However, in the transverse (T_1, T_2) subspace, Eqn. (S2) still holds, and we find only one low energy Goldstone mode: $\omega_q = Dq^2$ at small \vec{q} , which couples only to the inter-band P-H excitations at higher q (Fig. 3 (b)). By contrast, the remaining transverse mode is a gapped pseudo-Goldstone mode in SOC system.

¹ For the exact constraints on the pairing length from the spin-orbit coupled symmetries, see Yi-Xiang Yu, Jinwu Ye, Wu-Ming Liu, Phys. Rev. A 90, 053603 (2014).

² For the exact constraints on the correlation functions on a lattice from the spin-orbit coupled symmetries, see Fadi Sun, Jinwu Ye, Wu-Ming Liu, arXiv:1408.3399.